White Rose Research Online

eprints@whiterose.ac.uk
https://eprints.whiterose.ac.uk
Universities of Leeds, Sheffield and York

Deposited via The University of York.

White Rose Research Online URL for this paper:
https://eprints.whiterose.ac.uk/id/eprint/245668/

Version: Published Version

Article:
LAIRD, ALISON, DIGET, CHRISTIAN, ABRAHAMS, SOPHIE et al. (2026) Angular momentum drives proton-rich nucleosynthesis in hyperaccreting neutron stars in common envelopes. MONTHLY NOTICES OF THE ROYAL ASTRONOMICAL SOCIETY. stag1751. ISSN: 0035-8711

https://doi.org/10.1093/mnras/stag1751

Reuse
This article is distributed under the terms of the Creative Commons Attribution (CC BY) licence. This licence allows you to distribute, remix, tweak, and build upon the work, even commercially, as long as you credit the authors for the original work. More information and the full terms of the licence here: https://creativecommons.org/licenses/

Takedown
If you consider content in White Rose Research Online to be in breach of UK law, please notify us by emailing eprints@whiterose.ac.uk including the URL of the record and the reason for the withdrawal request.

UNIVERSITY OF LEEDS
University of Sheffield
UNIVERSITY of York

Monthly Notices of the ROYAL ASTRONOMICAL SOCIETY

MNRAS **552,** 1–11 (2026)
Advance Access publication 2026 October 6

https://doi.org/10.1093/mnras/stag1751

Angular momentum drives proton-rich nucleosynthesis in hyperaccreting neutron stars in common envelopes

Alexander D. Hall-Smith,[1★†] S. E. D. Abrahams,[1†] A. M. Laird,[1★†] C. Aa. Diget,[1] C. L. Fryer[2†] and S. W. Jones[2†]

[1]*School of Physics, Engineering and Technology, University of York, Heslington, York YO10 5DD, UK*
[2]*Center for Theoretical Astrophysics, Los Alamos National Laboratory, Los Alamos, NM 87545, USA*

Accepted 2026 August 10. Received 2026 August 5; in original form 2026 March 13

ABSTRACT

Interacting binaries, especially for massive star systems, produce a wide range of exotic systems including X-ray binaries and merging neutron star systems. In the rapid expansion as a star moves off the main sequence (core hydrogen exhaustion), the star can engulf its companion, forming a common envelope (CE) evolutionary phase. A CE phase where the engulfed star is a compact object (e.g. neutron star) can lead to rapid accretion on to the neutron star. Past work has focused on systems in which the accreting material has low angular momentum, studying turbulent outflows. This study instead focuses on accreting conditions where the accreting material has sufficient angular momentum to form a disc. Disc accretion systems lead to very different nuclear burning conditions, e.g. an increase in the time-scale on which nuclear burning can occur. This paper presents the results of nucleosynthesis modelling of material ejected from an accretion disc surrounding a 1.5 $M_\odot$ neutron star in a CE with a 15 $M_\odot$ companion. As material is accreted towards the neutron star sufficient heating will occur to eject a fraction of the material back into the surrounding envelope, producing a nucleosynthetic yield signature that differs from other explosion. We find that significant mass fractions of rp-process products are synthesized, thereby providing another mechanism for rp-process contribution to galactic chemical evolution, following ejection of the companion envelope. Furthermore, for later stages of the companion evolution, the accretion of helium leads to alpha-rich nucleosynthesis, resulting in supernova-like nucleosynthesis, producing in particular ^{44}Ti and ^{56}Ni. Further work on modelling both the accretion disc wind and the companion envelope ejection is vital to understand the contributions of these scenarios to chemical evolution.

Key words: accretion, accretion discs – nuclear reactions, nucleosynthesis, abundances – stars: neutron.

1 INTRODUCTION

Common envelope (CE) evolution occurs when one of the stars in a binary systems begins to expand (typically after hydrogen- or helium-burning exhaustion). During this expansion, the star can drive such rapid mass transfer on its companion that the companion is overwhelmed, and the system ultimately develops an atmosphere that surrounds (or envelops) both the core of the expanding star and its companion (for a review, see N. Ivanova et al. 2013; N. Ivanova, S. Justham & P. Ricker 2020). The frictional drag caused by this envelope leads to the loss of angular momentum in the core-companion orbit, tightening the binary. Many of the close binaries observed in the Universe will or have gone through a CE phase and this phase is critical in the formation of everything from X-ray binaries and recycled pulsars (N. Ivanova et al. 2008) to the progenitors of type I supernovae (X. Meng & P. Podsiadlowski 2017) and gamma-ray bursts (C. L. Fryer, S. E. Woosley & D. H. Hartmann 1999).

For massive star binaries, systems can go through more than one CE phase. When the more massive star evolves off the main sequence branch, it can expand and undergo Roche Lobe overflow, transferring mass to the less massive companion. This CE phase tightens the binary, making it more likely to remain bound after the supernova explosion that the more massive star undergoes at the end of its life. The remnant of this supernova explosion can be a neutron star. When the less massive companion evolves off the main sequence, it can envelope the neutron star and another CE phase begins. The neutron star accretes material as it inspirals through the companion, and this accretion can drive outflows (N. Ivanova et al. 2013). If the neutron star spirals into the companion's core, the angular momentum of the core is likely to produce a rapidly accreting disc that may produce a gamma-ray burst (C. L. Fryer & S. E. Woosley 1998; W. Zhang & C. L. Fryer 2001; C. L. Fryer et al. 2013), a subclass of gamma-ray bursts known as ultra-long duration gamma-ray bursts (C.

★ E-mail: alexander.hall-smith@york.ac.uk (ADH-S); alison.laird@york.ac.uk (AML)
† NuGrid Collaboration (http://nugridstars.org).

© The Author(s) 2026.
Published by Oxford University Press on behalf of Royal Astronomical Society. This is an Open Access article distributed under the terms of the Creative Commons Attribution License (https://creativecommons.org/licenses/by/4.0/), which permits unrestricted reuse, distribution, and reproduction in any medium, provided the original work is properly cited.

Downloaded from academic.oup.com/mnras/article/552/4/stag1751/8869235 by guest on 16 October 2026

C. Thöne et al. 2011; E. Neights et al. 2026) or fast blue optical transients (J. Klencki & B. D. Metzger 2026). Even if the compact object does not spiral into the stellar core, it is likely that these systems form jets that drive outflows with supernova-like outbursts (N. Ragoler et al. 2022). A growing number of multidimensional simulations have studied the accretion and its outflow (e.g. S. Hillel, R. Schreier & N. Soker 2022; M. Vetter et al. 2024; A. L. Juarez-Garcia et al. 2025; R. Schreier, S. Hillel & N. Soker 2025).

Knowing that these mergers eject mass that has been processed through close interactions with a neutron star, it is important to understand the detailed yields from these mergers. Based on the properties of these accretion discs (R. Popham, S. E. Woosley & C. Fryer 1999), R. Surman, G. C. McLaughlin & W. R. Hix (2006) calculated the yields, finding that only in the highest accretion rates could these discs produce considerable r-process elements. Several nucleosynthetic studies have studied non-rotating (C. L. Fryer et al. 2006; J. Keegans et al. 2019; P. Anninos et al. 2026) accretion scenarios. In a non-rotating system, the material accreting on to the neutron star is expected to develop an unstable entropy profile, driving vigorous convection (R. A. Chevalier 1989, 1993) that could produce outflows (C. L. Fryer et al. 2006). The temperatures achieved near the surface of the neutron are sufficiently high to drive strong nuclear burning. J. Keegans et al. (2019) studied the yields of these outflows, assuming that the time spent at extreme temperatures and densities was limited to a single turnover time. The minimal time spent at these extreme conditions limits the type of yields that can be produced. In detailed hydrodynamic models, P. Anninos et al. (2026) found that, in the complex convective motion near the neutron star, the ejected material can spend much more time in extreme, nuclear-burning conditions.

At extremely high accretion rates, neutrino emission and absorption can be important. Except for the simulations of C. L. Fryer et al. (2006), these calculations neglected the role of neutrino absorption in setting the electron fraction. In supernovae, this neutrino absorption tends to reset the electron fraction (C. Fröhlich et al. 2005; A. Sieverding, D. Kresse & H.-T. Janka 2023) leading to ejecta with electron fractions near 0.5. As the material expands out of nuclear statistical equilibrium, there is little time for burning pathways with long wait times and most of the ejecta is limited to iron peak elements with only trace amounts of elements produced with atomic weights heavier than 90–100.

Angular momentum can dramatically change this picture. Given the expected accretion of angular momentum, it is likely that discs form, changing the temperature and density evolution of the ejected material. Material accreting through a disc can spend much more time at sufficiently high temperatures for nuclear burning, leading to the production of heavy elements that cannot be produced in a single convective turnover time. Many disc studies have focused, like R. Surman et al. (2006), on the r-process yield from neutron-rich ejecta. This requires the material to be held at extreme densities/temperatures for sufficient time for electron capture to deleptonize the material. As we shall see here, and as discussed in preliminary results by S. E. D. Abrahams et al. (2023), proton-rich material is more common in many CE cases.

The scenario investigated in this study consists of a 15 $M_\odot$ massive star, at the end of core hydrogen burning, as it expands to engulf a 1.5 $M_\odot$ neutron star and forms a CE system. As the neutron star inspirals towards the core of its massive-star companion, it will accrete material and move from the hydrogen-rich outer shell towards the helium-rich core. This allows for a wider range of nucleosynthesis processes than originally considered by J. Keegans et al. (2019) – which modelled the neutron star only accreting solar abundance material.

2 NEUTRON STAR ACCRETION DISC TRAJECTORIES

Depending upon the amount of angular momentum in accreting material, the nature of the accretion and mass ejection of a neutron star in a CE can behave very differently. Yield calculations require 'trajectories' that describe the evolution of the density and temperature with time. If the angular momentum is negligible, convection produces single (J. Keegans et al. 2019) or multiple (P. Anninos et al. 2026) cycles to describe the trajectory evolution. Density and velocity gradients in massive stars will lead to a modest amount of angular momentum accreted in the flow. In this paper, we focus on models where this angular momentum is sufficient to form a disc (e.g. $5 \times 10^{16-17}$ cm^2 s^{-1}). The trajectory evolution for this disc scenario can be described in three phases: infall on to the disc, disc evolution, and disc-wind ejection.

For the infall phase, we assume the material accretes at free-fall. In this scenario, the infall velocity is set to the free-fall velocity ($v_{\rm ff}$):

$$v_{\rm ff} = (2GM_{\rm NS}/r)^{1/2} \quad (1)$$

where r is the infall radius, G is the gravitational constant, and $M_{\rm NS}$ is the neutron star mass. We assume adiabatic contraction and the material heats up as it falls inward. This phase persists until the angular momentum in the material halts the infall, causing it to hang up in a disc. The material hangs up at a radius ($r_{\rm disc}$) when the centrifugal force equals the gravitational force:

$$r_{\rm disc} = j_{\rm ang}^2/(GM_{\rm NS}) \quad (2)$$

where $j_{\rm ang}$ is the specific angular momentum of the accreting material. We assume angular momentum conservation in the collapse so $j_{\rm ang} = 10^{17}$ cm^2 s^{-1} corresponds to a 10 km s^{-1} asymmetry at 10^{11} cm.

Disc evolution is approximated by an α disc model (N. I. Shakura & R. A. Sunyaev 1973). We assume the accretion rate in the disc is set by the infall accretion rate (e.g. Bondi–Hoyle–Lyttleton or a reduced Bondi–Hoyle accretion; H. Bondi 1952; M. Ruffert & U. Anzer 1995; R. W. Everson et al. 2020). With the α disc prescription, we can estimate the accretion time-scale:

$$t_{\rm disc} = P_{\rm disc}/\alpha, \quad (3)$$

where $P_{\rm disc} = 2\pi r_{\rm disc}^{3/2}(GM_{\rm NS})^{-1/2}$ and $\alpha = 0.01$-0.1. α is a simplified parametrization of the viscous forces in the disc that transport angular momentum and eject matter from the disc. For material accreting on to to a 1.4 $M_\odot$ neutron star with an angular momentum, $j_{\rm ang} = 10^{17}$ cm^2 s^{-1}, the disc initially hangs up at $r_{\rm disc} = 50$ km with a disc accretion time-scale of 1.8–18 s (it can be 125 times longer if the angular momentum is five times larger). As this time is much shorter than the evolution in the CE, we can assume that it is instantaneous. For the structure of the disc, we leverage the analytic models by R. Popham et al. (1999).

Although the accretion time is short when compared to the evolution of a CE, it is long compared to most convective-burning time-scales. The trajectories explored in J. Keegans et al. (2019) and P. Anninos et al. (2026) operate on the time-scale of milliseconds, while trajectories here last over 2000 s as a result of inclu-

Downloaded from academic.oup.com/mnras/article/552/4/stag1751/8869235 by guest on 16 October 2026

sion of angular momentum. The time-scale on which accretion, disc evolution, and ejection occur are also an order of magnitude longer than typical X-ray burst (XRB) time-scales. While XRB can reach peak temperatures of 1–1.9 GK, models explored here can reach peak temperatures of 8 GK (A. Parikh et al. 2008).

Despite many disc calculations, the exact nature of disc accretion and subsequent disc wind remains a matter of active study. Some models argue that the viscosity can drive mass-loss across the entire disc, others argue that the mass ejection occurs primarily at the inner disc radius (M. A. R. Kaltenborn et al. 2023). For our models, we typically assume the wind ejecta is uniformly distributed across the disc. When the material is blown off in a wind, it accelerates roughly to the escape velocity of the material. For this final phase of our trajectory, we assume an exponential + power-law evolution. For explosive supernova and r-process yields, typical trajectories invoke either acceleration or free-streaming regimes. As the ejecta accelerates, the material slowly expands, causing the density (ρ) to drop, following an exponential:

$$\rho = \rho_0 e^{-t/\tau}, \tag{4}$$

where ρ_0 is the density at time 0 and τ is the dynamical time-scale related to the acceleration. If we further assume the entropy (S) is constant and radiation pressure dominates, $S \propto T^3/\rho$, the temperature (T) is given by

$$T = T_0 e^{-t/(3\tau)}, \tag{5}$$

where T_0 is the temperature at time 0. Once the velocity accelerates to its peak velocity, we assume the ejecta moves outward at a constant velocity (producing the homologous outflows used in supernova light curves). With this assumption, the density and temperature follow power-law trajectories:

$$\rho = \rho_0 (t/\tau)^{-3}, \tag{6}$$
$$T = T_0 (t/\tau)^{-1}, \tag{7}$$

where τ is the expansion timescale based on the ejecta velocity. We transition from an exponential to power-law expansion at three times this expansion time-scale.

A sample of the trajectories produced in this three-phase formalism is shown in Fig. 1 using our high angular momentum models and an $\alpha = 0.01$. The angular momentum of the accreting material produces a long-lived disc phase (over 1000 s). This long-lived disc evolution phase can be split into two sections. The plateau section is the sub-gigakelvin temperature region, where material first enters the edge of the accretion disc and begins to lose angular momentum. The peak section is a rapid temperature increase as the material reaches its disc ejection radius relative to the neutron star. As the material moves through the disc, it is compressed further due to the gravitational effects of the neutron star, therefore increasing the drag forces and further dissipating the angular momentum, leading to the exponential increase in temperature, until the material is ejected. The final amount of ejected material that is mixed back into the companion's envelope is a fraction of the total material that entere the accretion disc (M. A. R. Kaltenborn et al. 2023). Wind mass-loss ejection fractions can range from 7 per cent up to 40 per cent depending on the entropy and wind treatment. Due to the extremely high density of the accretion disc, which is between one to three orders of magnitude larger than the surrounding medium, throughout the evolution of the CE phase, we assume that the accretion disc remains largely unaffected as it passes through the companion medium. For nuclear burning in CEs, the yields appear to be insensitive

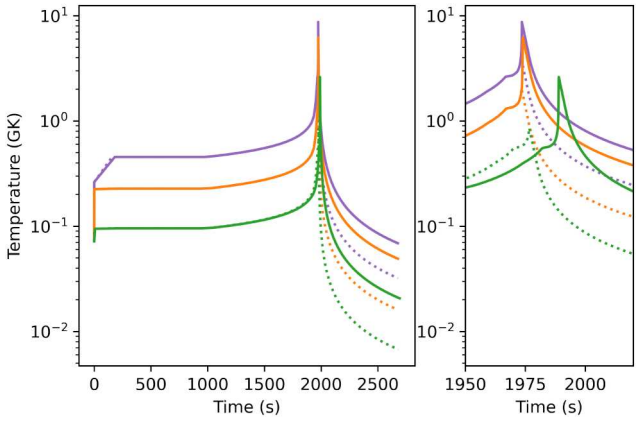


Figure 1. The temperature evolution of three different accretion rate trajectories: 1×10^{-5} $M_\odot s^{-1}$ (green), 32×10^{-5} $M_\odot s^{-1}$ (orange), and 512×10^{-5} $M_\odot s^{-1}$ (purple). These are split into three phases: the infall phase (rapid increase at $t = 0$), the disc evolution (plateau and increase to peak), and the ejection phase (rapidly cooling post-peak). The temperature evolution of material ejected near the disc edge is shown in dotted lines and the material ejected close to the neutron star is shown in solid lines.

to the nature of the first (infall) phase of our trajectories. The free-fall phase evolves quickly and the temperatures and densities tend to be sufficiently low that little burning occurs. The yields are most sensitive to the disc evolution stage. At the beginning of the ejection phase, the temperature and densities are still sufficiently high for nuclear burning to occur, as the temperature continues to decrease through the ejection phase the material quickly cools and decay processes dominate.

We assume that the neutron star accretion disc ejects material into the CE at a constant rate across the disc surface. The final mass fraction distribution from each point of ejection, for a single accretion rate, were therefore averaged to produce a final mass fraction distribution for that accretion rate. This averaging provides insight into the composition of the material that is ejected back into the CE. To understand how material is being processed in the accretion disc we look at the instantaneous reaction flux and isotopic evolution for a trajectory with an individual point of ejection.

Table 1 shows the range of peak temperatures reached in each trajectory, as well as the temperature at the edge of the accretion disc. The plateau temperatures of each accretion rate are above the threshold for CNO nuclear burning. This will provide a mechanism for material to be processed into heavier isotopes before the peak temperature is reached.

Neutrino emission and absorption can vary the electron fraction in rapidly accreting disc calculations. However, for the low accretion rates used in this study, the deleptonization from electron capture and any neutrino absorption is minimal. We will discuss this in more detail in a later paper.

3 COMPANION STAR DETAILS

The companion star plays a significant role in both the evolution of the CE system and the type of material that is accreted around the neutron star. The stellar evolution of a 15 $M_\odot$ zero-age main sequence (ZAMS) star with metallicity of 2 per cent from C. Ritter et al. (2018) was used to calculate the composition and accretion rate at various points through the expansion phase of the star.

Downloaded from academic.oup.com/mnras/article/552/4/stag1751/8869235 by guest on 16 October 2026

Table 1. Details of trajectories studied in this work. The first column shows the accretion rate that feeds the accretion disc, the second column shows the range of distances from the centre of the neutron star where material is ejected, the third column shows the temperature of the material as it orbits in the edge of the accretion disc, and the final column shows the peak temperature range of the material before it is ejected.

Accretion rate ($M_\odot$ s^{-1})	Range of ejection ($\times 10^6$ cm)	Plateau temperature (GK)	Peak temperature range (GK)
1×10^{-5}	1.0422–4.9695	0.094	0.86–2.61
16×10^{-5}	1.0422–4.9695	0.191	1.71–5.23
32×10^{-5}	1.0422–4.9696	0.224	2.04–6.21
512×10^{-5}	2.0355–4.9695	0.454	4.07–8.72

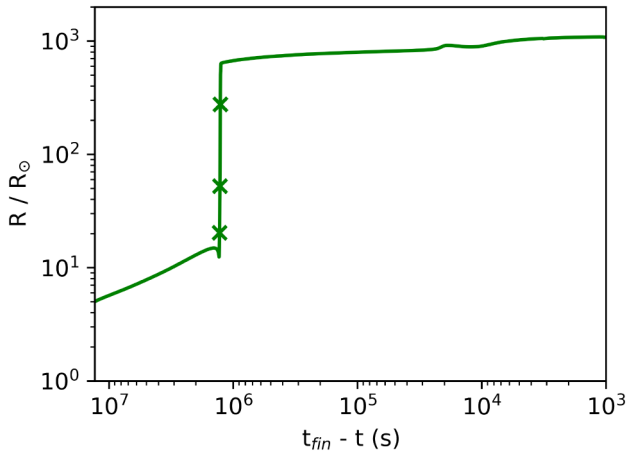


Figure 2. Evolution of the 15 $M_\odot$ companion. The *x*-axis shows the time remaining until core collapse and the *y*-axis shows the radius of the companion. The markers show the time during the companion evolution at which we modelled the CE events. The companion ages used are 1.256×10^7, 1.257×10^7, and 1.258×10^7 yr.

Specifically, when the core of the star begins to deplete hydrogen at its centre through the CNO cycle, helium is produced in the core and the star begins to contract. This contraction causes heating, which in turn triggers shell hydrogen burning. The increased energy output from hydrogen shell burning further drives an expansion of the stellar envelope (C. Iliadis 2007).

The evolution of the 15 $M_\odot$ companion is shown in Fig. 2; the three points on the line show the points during expansion where the compositions at specific accretion rates were calculated. As the neutron star accretes material, a velocity and density gradient will form across the accretion disc (M. MacLeod & E. Ramirez-Ruiz 2015). These gradients will limit the rate at which material accretes. To account for this, the accretion rate calculated for each point in the companion star is multiplied by a non-dimensional parameter $\lambda_{\rm BHL}$. In this work, $\lambda_{\rm BHL} = 0.1$. The inclusion of the parameter $\lambda_{\rm BHL}$ follows J. Keegans et al. (2019), where $\lambda_{\rm BHL}$ had a upper and lower value: 0.25 and 0.025, respectively.

During this phase of rapid expansion, three companion sizes (ages) were used to calculate the initial composition of the material entering the neutron star accretion disc; 20.3 $R_\odot$ (1.256×10^7 yr), 52.4 $R_\odot$ (1.257×10^7 yr), and 275.6 $R_\odot$ (1.258×10^7 yr). These three radii were chosen as the formation of the CE will depend on the orbital separation of the neutron star and its companion. If they are close, the CE will form early on during the expansion phase; if they are distantly separated, it will form at the end. As the neutron star plunges towards the companion core, it will accrete material the entire time; however, material accreted early on in the plunge in phase is not dense and does not reach high enough temperatures for interesting nucleosynthesis to occur. Once the neutron star is within 5 solar radii the mass transferred is sufficient to produce the high temperature and density medium that result in complex nucleosynthesis. The accretion rates investigated in this study range between 1×10^{-5} and 512×10^{-5} $M_\odot s^{-1}$, which produce peak temperatures between 0.856 and 8.72 GK.

4 NUCLEOSYNTHESIS CALCULATIONS AND REACTION NETWORK

As the neutron star accretion disc is a high temperature and density environment, ranging from 0.25 GK and 1 g cm^{-3} near the edge of the accretion disc up to 8.72 GK and 3.29×10^8 g cm^{-3} near the neutron star surface, it leads to a variety of different types of nucleosynthesis. The environment also rapidly changes as the material/evolves through the accretion disc and is then ejected. To ensure that the large variety of potential reaction pathways and rapid changes in the temperature and density are correctly modelled the nucleosynthesis network, the NuGrid tool PPN[1] (M. Pignatari et al. 2016) was used to post-process each trajectory. This utilized an isotopic network spanning from neutrons and protons up to ^{216}Po including all isotopes with a half-life greater than 5×10^{-6} s. This decay limit was chosen as the smallest time-steps in the trajectories are 1×10^{-5} long. This allows short-lived isotopes that would decay before the end of the scenario to be identified. This results in a network of 5234 isotopes split across the valley of stability. A large network was used as the high temperature leads to production of exotic nuclei away from stability.

The reaction rate data used in NuGrid comes primarily from the Joint Institute for Nuclear Astrophysics Center for the Evolution of the Elements, JINA-CEE, Reaclib compilation (R. H. Cyburt et al. 2010). By default, NuGrid is designed to use JINA-CEE Reaclib v1.1, published in April 2013, which is no longer up to date. To ensure that the correct reaction data were used, the JINA-CEE Reaclib default compilation, published in June 2021, was used in place of Reaclib v1.1. The Reaclib library does not cover the entire network of reactions and so is supplemented with neutron capture rates from the Karlsruhe Astrophysical Database of Nucleosynthesis in Stars (KADoNiS) (I. Dillmann et al. 2008), as well as beta decay rates by T. Oda et al. (1994) and K. Langanke & G. Martínez-Pinedo (2000).

5 INITIAL MASS FRACTION VARIATIONS

The position of the neutron star inside the companion envelope will impact the composition of the accreted material. Fig. 3 shows how the mass fractions of ^{2}H, ^{4}He, ^{12}C, ^{14}N, and ^{16}O vary with

[1] https://nugrid.github.io/

Downloaded from academic.oup.com/mnras/article/552/4/stag1751/8869235 by guest on 16 October 2026

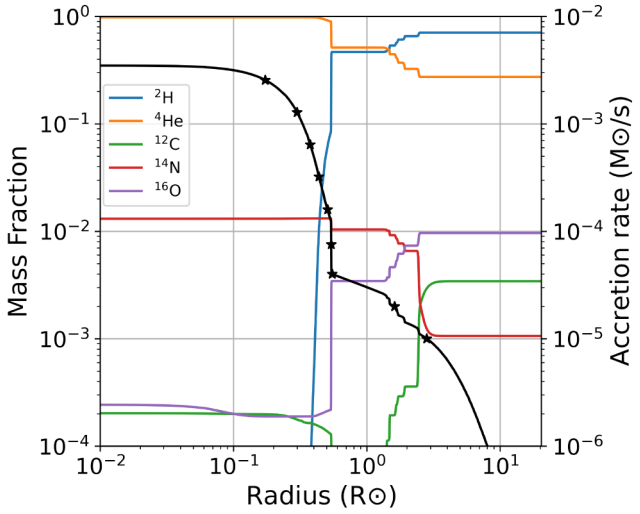


Figure 3. Composition of a 15 $M_\odot$ ZAMS star, when it has expanded to 20.3 $R_\odot$. The mass fraction (left axis) for ^{2}H, ^{4}He, ^{12}C, ^{14}N, and ^{16}O shown as a function of radial distance from the companion core. Also shown is the accretion rate (right axis) in solar masses per second versus radial distance. Black asterisks indicate accretion rates used in current study.

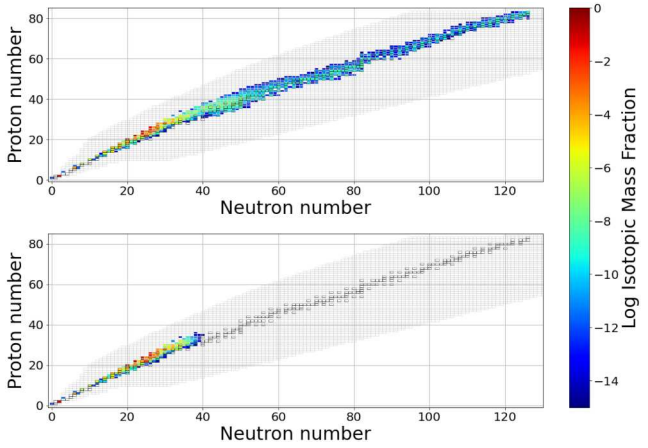


Figure 4. Final isotopic mass fractions for a 1.5 $M_\odot$ neutron star accreting 32×10^{-5} $M_\odot$ s^{-1} from a 15 $M_\odot$ companion. The bottom figure shows the resulting isotopic distribution when using an initial composition taken from C. Ritter et al. (2018) MESA models (170 isotopes between ^{1}H and ^{62}Ni). The top shows the resulting isotopic distribution when using the initial composition from C. Ritter et al. (2018) and including all solar seed nuclei (389 isotopes between ^{1}H and ^{209}Bi).

respect to radial position inside the companion envelope, as well as how the accretion rate varies throughout the 20.3 $R_\odot$ 15 $M_\odot$ companion after core hydrogen burning has finished but before core helium burning begins. This clearly shows that the highest accretion rates, 32×10^{-5} to 256×10^{-5} $M_\odot$ s^{-1}, can only be achieved inside the helium core; therefore, the material entering the accretion disc will have the same composition as the companion core.

The initial composition for each accretion rate was calculated using MESA stellar evolution models by C. Ritter et al. (2018). Using the evolution of a 15 $M_\odot$ star, the internal structure and composition were taken at three times post core hydrogen burning. We model only the plunge in phase of the CE evolution, as defined by N. Ivanova et al. (2020), as this is the most studied and well known phase (J.-C. Passy et al. 2012). During this phase, the neutron star evolves through the companion envelope towards the core, transitioning through internal structures of the companion and reaching higher accretion rates and varying the composition of material entering the accretion disc. The initial compositions used contained 170 isotopes between ^{1}H and ^{62}Ni taken from MESA, with solar seed nuclei up to bismuth from NuGrid stellar yields, both taken from C. Ritter et al. (2018).

It is important to include the full range of initial seed nuclei. Fig. 4 shows the resulting final isotopic distribution when using only the 170 isotopes used from C. Ritter et al. (2018) MESA models (bottom) compared to the 389 isotopes initial composition containing all stable solar seed nuclei up to bismuth. Without the inclusion of these heavy seeds, nucleosynthesis only occurs in the low-mass region, but with the heavy seeds included there is nucleosynthesis throughout the chart of nuclei.

6 NUCLEOSYNTHESIS DURING COMMON ENVELOPE EVOLUTION

All of the data presented in this section utilize a single value for the angular momentum of the accreted material, 1×10^{17} cm^2 s^{-1}, and therefore for a single size of accretion disc. As part of this work, we studied the effect of changing the angular momentum of accreted material. Decreasing the angular momentum of the accreted material by a factor of 10 results in a longer plateau time, therefore producing more CNO and CNO breakout isotopes. However, as the nuclear burning is most sensitive to the peak temperature, the resulting isotopic and elemental distributions still follow the same trends as those in the high angular momentum case.

6.1 Hydrogen-rich outer envelope region

A CE evolves when the companion star first undergoes expansion to a radius of 20.3 $R_\odot$. The lowest accretion rate studied is 1×10^{-5} $M_\odot$ s^{-1}. Fig. 3 shows that the neutron star accretes material from the bottom of the hydrogen burning shell. The initial composition consists of 70.6 per cent hydrogen, with stable nuclei and trace amounts of ^{13}N, ^{15}O, and ^{22}Na that are produced during the lifetime of the companion. ^{13}N and ^{15}O are produced during the CNO cycle inside the companion, ^{22}Na is produced through proton captures and has a half-life of 2.6 yr. Fig. 5 shows the averaged mass fraction of isotopes ejected throughout the accretion disc. The high abundance of protons combined with the high temperature and density through out the trajectory (see Fig. 1) results in the synthesis of neutron deficient material. There is evidence of material reaching the SnSbTe cycle, as the mass fractions of isotopes below the SnSbTe cycle have comparatively high mass fractions.

Flux plots are utilized to investigate the reaction flow of material at three points during this trajectory, at temperatures of 0.5 GK (Fig. 6), 1 GK (Fig. 7), and the peak temperature of the trajectory which is 1.8 GK (Fig. 8). For the full temperature evolution of this trajectory, see Fig. 1.

Fig. 6 shows the reaction flux as material reaches 0.5 GK. At this temperature the reaction flux clearly shows the hot CNO cycle and the breakout reaction $^{15}O(\alpha,\gamma)^{19}Ne$ have high reaction fluxes. Proton capture chains do not reach the proton drip line, as shown by the balanced proton capture and proton emission reactions at ^{25}Si, ^{30}S, and ^{42}Ti. Proton captures reach up to ^{56}Fe,

Downloaded from academic.oup.com/mnras/article/552/4/stag1751/8869235 by guest on 16 October 2026

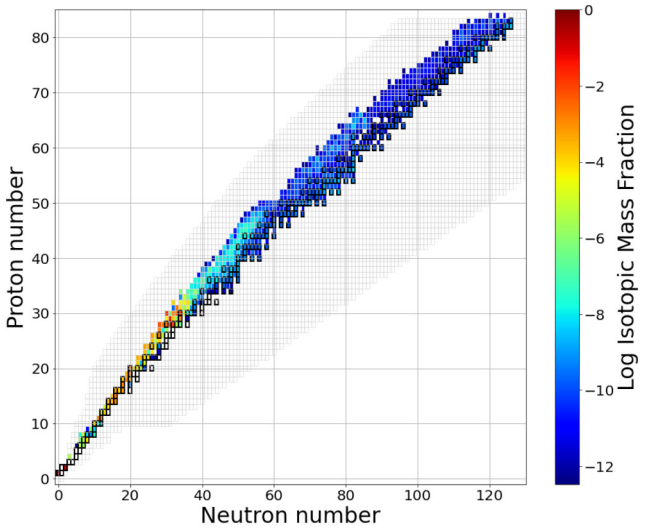


Figure 5. Average undecayed final isotopic distribution from the 1×10^{-5} $M_\odot$ s^{-1} accretion rate trajectory. Average over disc ejection radius (1.0422×10^6 to 4.9695×10^6 cm). Stable nuclei shown in black boxes.

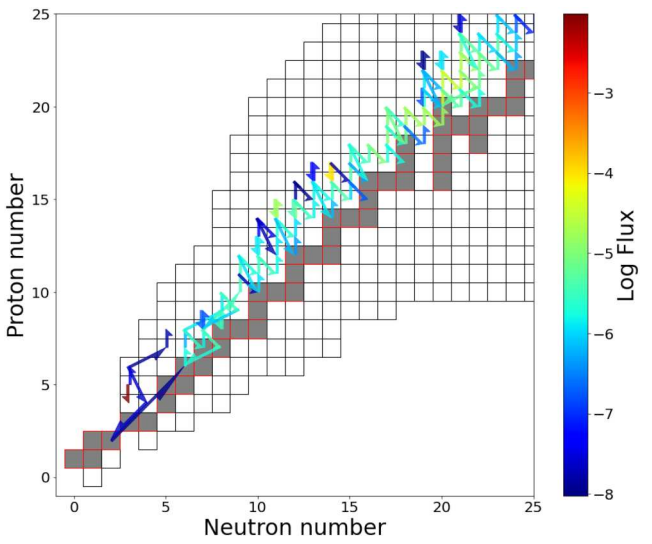


Figure 6. Reaction flux through the 1×10^{-5} $M_\odot$ s^{-1} accretion rate trajectory for the 2.0355×10^6 cm disc ejection radius at 0.5 GK, before the peak temperature is reached, showing the HCNO cycle breakout to rp-process. The initial composition was solar-like.

but cannot process material further due to competing beta decay reactions.

Fig. 7 shows the reaction flux at 1 GK, before the peak temperature is reached. We see that the main nucleosynthesis pathways have changed when compared to Fig. 6. At this higher temperature, alpha capture reactions begin to have a significant role in producing heavier isotopes. The ^{18}Ne$(\alpha, p)^{21}$Na, ^{22}Mg$(\alpha, p)^{25}$Al, and ^{26} si$(p, \gamma)^{27}$P reactions provide a pathway for material to escape the hot CNO cycle and enter the rp-process. Between magnesium and chlorine, the reaction channels compete between alpha capture and proton captures. Beyond chlorine, proton capture reactions are the main source of nucleosynthesis. When compared to Fig. 6, we see that material is reaching further into the neutron deficient region and the competing proton capture and beta decay channels are further from the valley of stability. At this

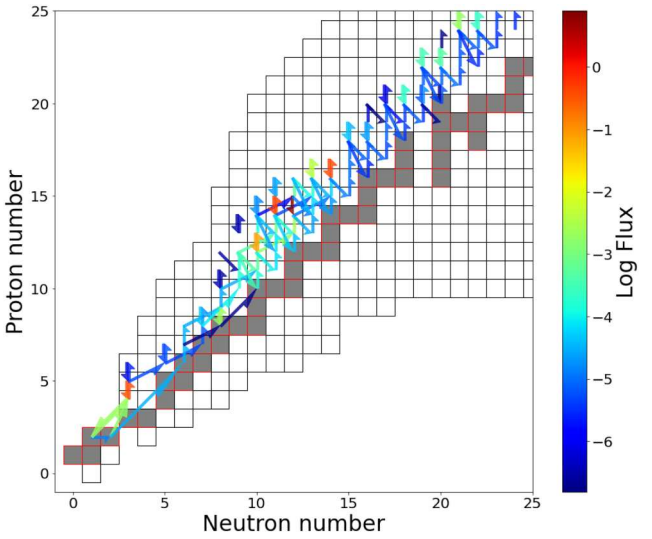


Figure 7. Reaction flux through the 1×10^{-5} $M_\odot$ s^{-1} accretion rate trajectory at 1 GK before the peak temperature is reached.

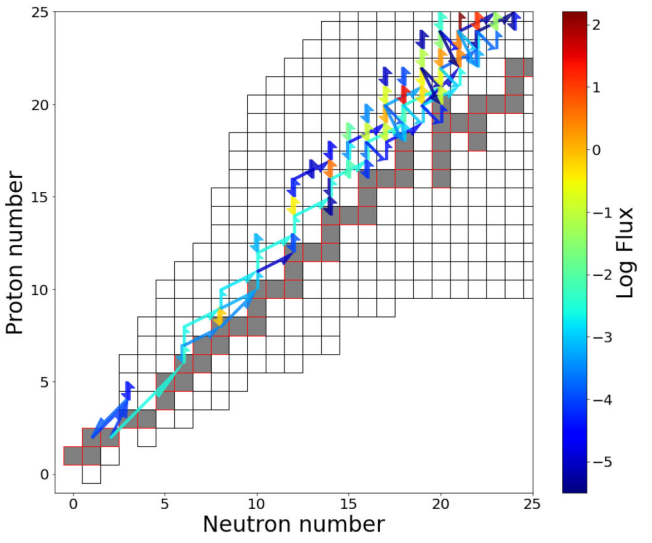


Figure 8. Reaction flux through the 1×10^{-5} $M_\odot$ s^{-1} accretion rate trajectory at the peak temperature, 1.8 GK.

temperature, proton capture reactions extend past the iron group up to gallium and germanium, but do not extend to the SnSbTe cycle isotopes.

Fig. 8 shows the reaction flux at the peak temperature, 1.8 GK. The extreme temperature and presence of both helium and hydrogen result in a combination of (α, p), (α, γ), and (p, γ), which drive nucleosynthesis up to phosphorus. Beyond phosphorus, nucleosynthesis is dominated by proton capture reactions. Proton captures reach the SnSbTe cycle isotopes at the peak temperature, as shown in Fig. 5.

Fig. 9 shows the isotopic evolution of ^{12}C, ^{14,15}O, ^{18}Ne, and ^{100}Cd for the entire length of the trajectory (left), and zoomed in around the peak temperature (right). ^{12}C is slowly destroyed and ^{14}O and ^{15}O are produced via the CNO cycle during the lead up to the peak temperature. At the peak temperature, these isotopes are destroyed via proton and alpha capture reactions. Due to the high availability of protons and high temperature after material

Downloaded from academic.oup.com/mnras/article/552/4/stag1751/8869235 by guest on 16 October 2026

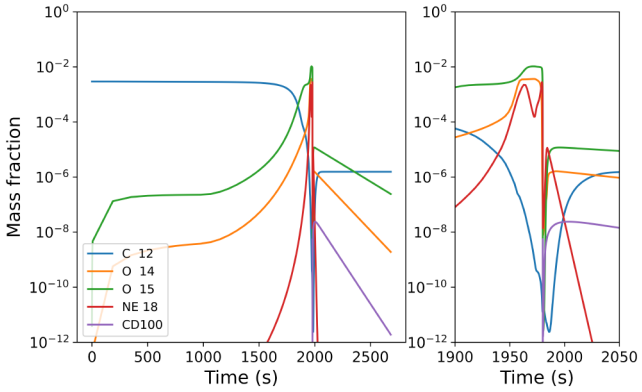


Figure 9. Isotopic evolution of isotopes around CNO during 1×10^{-5} $M_\odot$ s^{-1} accretion rate trajectory. ^{100}Cd is included showing that the rp-process reaches the SnSbTe cycle.

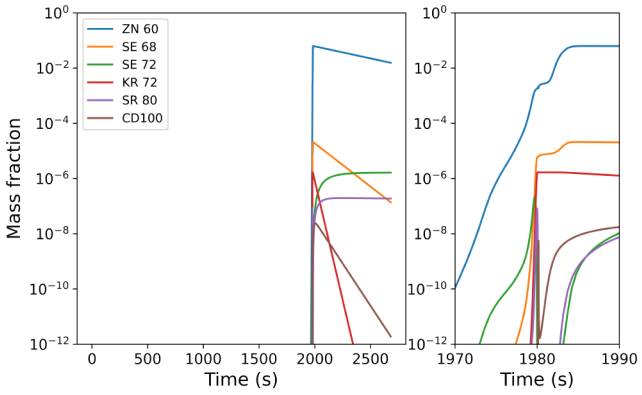


Figure 10. Isotopic evolution of heavy rp-process waiting point isotopes during 1×10^{-5} $M_\odot$ s^{-1} accretion rate trajectory. ^{100}Cd is included as this shows the rp-process reaching the SnSbTe cycle.

has reached, its disc ejection radius (peak temperature) relative to the neutron star, ^{12}C and ^{15}O are produced again as the CNO cycle is able to continue processing material during the disc ejection phase. ^{100}Cd is produced during the peak temperature of the trajectory. The sharp peak at 1980 s shows ^{100}Cd being produced and then immediately destroyed as proton captures process material through ^{100}Cd. Shortly after the peak temperature (approximately 10 s after) of the trajectory, the mass fraction of ^{100}Cd increases as a result of β^+ decays on the isobar (right panel of Fig. 9). This indicates that nucleosynthesis of reached the SnSbTe cycle before it is ejected. As ^{100}Cd is radioactive, it then decays to stability as material is ejected from the neutron star accretion disc.

Fig. 10 provides further evidence that the high mass fraction of ^{100}Cd in Fig. 9 and high undecayed final mass fraction of isotopes below the SnSbTe cycle in Fig. 5 are as a result of rp-process nucleosynthesis. ^{60}Zn, ^{68} se, ^{72}Kr, and ^{80} sr are rp-process waiting point isotopes and material accumulates at these isotopes during rp-process nucleosynthesis. The right panel of Fig. 10 shows the rapid production and destruction of ^{72}Se, ^{80}Sr, and ^{100}Cd at the peak temperature as material is processed through these isotopes towards the proton drip line. It also shows that the mass fraction of ^{60}Zn increases followed by that of ^{68} se, followed by ^{72}Kr as the peak temperature of the trajectory is reached. This is evidence of material moving through these isotopes during the rp-process, leading to production of ^{100}Cd. Overproduction of p-nuclides is

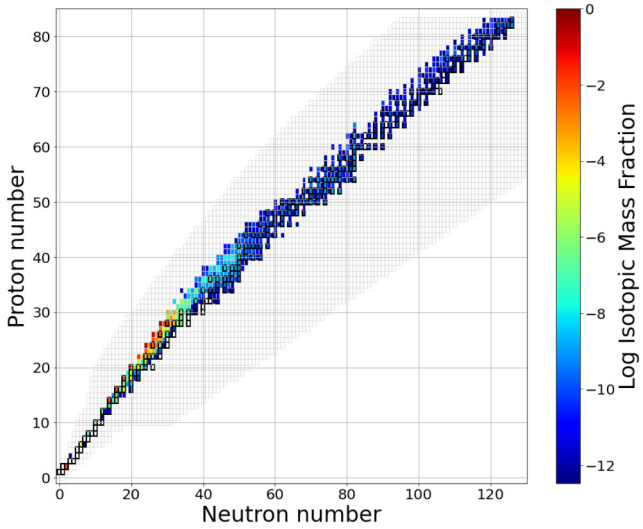


Figure 11. Average final isotopic distributions from the 32×10^{-5} $M_\odot$ s^{-1} accretion rate trajectory.

observed in these trajectories, as explored by Abrahams et al. (in preparation).

6.2 Mixed hydrogen and helium region

When the neutron star has inspiralled further into the envelope of the 20.3 $R_\odot$ early expansion phase companion, it begins to accrete material from the mixed boundary between the hydrogen shell and helium core. The neutron star accretes material at 32×10^{-5} $M_\odot$ s^{-1} (see Fig. 3). Trajectories with this accretion rate have a peak temperature ranging between 2 GK for material ejected near the edge of the disc and 6.21 GK for material ejected near the neutron star (see Fig. 1). The final isotopic abundance for material ejected from the accretion disc at this point in the companion star is shown in Fig. 11. When compared to the averaged mass fractions ejected from the 1×10^{-5} $M_\odot$ s^{-1}, with peak temperatures ranging from 0.856 to 2.61 GK (see Fig. 5), we can see that neutron deficient nuclei are produced, but not to the same extent. The bulk of material is trapped in the iron peak elements and nucleosynthesis does not reach the SnSbTe cycle. The final mass fraction of alpha capture products such as ^{28}Si, ^{32}S, ^{36}Ar, ^{40}Ca, and ^{44}Ti are much higher than the surrounding isotopes, indicating alpha capture reactions drive nucleosynthesis up to the iron group elements.

Fig. 12 shows the reaction flux through material accreted during the 32×10^{-5} $M_\odot$ s^{-1} trajectory when the temperature evolution reaches 2 GK. Alpha captures dominate in the lower mass region, due to the high abundance of alpha particles and the extreme temperatures, which result in successive alpha captures from ^{12}C up the iron group, leading to the high final mass fractions of ^{28}Si, ^{32}S, ^{36}Ar, ^{40}Ca, and ^{44}Ti. Beyond titanium, before the iron group elements, proton capture reactions begin to compete with alpha captures and become the preferred reaction pathway. Beyond iron nucleosynthesis is dominated by proton capture reactions, producing neutron deficient isotopes up to molybdenum. However, due to the reduced availability of protons nucleosynthesis is limited in this region and does not reach up to the SnSbTe cycle.

To better understand the nucleosynthesis occurring inside the disc, the isotopic evolution of alpha capture isotopes ejected

Downloaded from academic.oup.com/mnras/article/552/4/stag1751/8869235 by guest on 16 October 2026

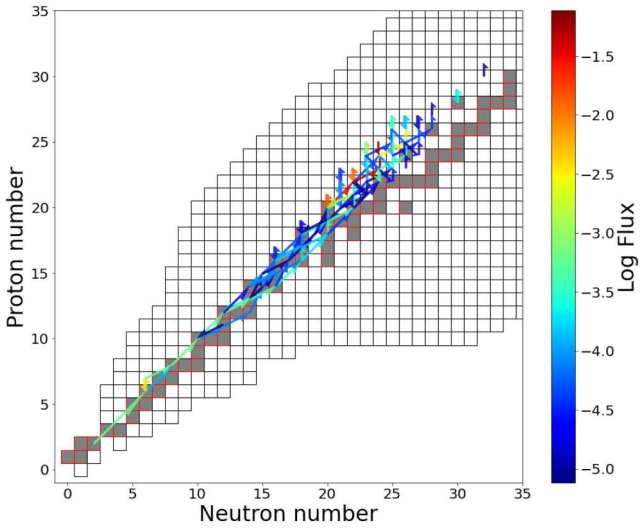


Figure 12. Reaction flux through the 32×10^{-5} $M_\odot$ s^{-1} accretion rate trajectory at 2 GK before the peak temperature is reached. This clearly shows the alpha capture process up to ^{44}Ti. At this temperature, the CNO cycle is bypassed by alpha capture reactions.

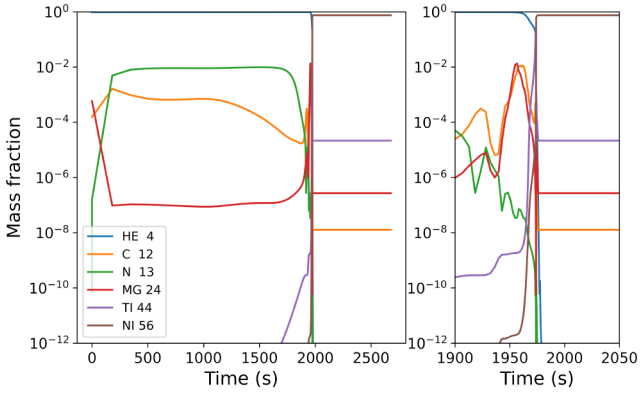


Figure 13. Isotopic evolution of alpha capture products ejected at 2.0355×10^6 cm from the centre of the accretion disc during the 32×10^{-5} $M_\odot$ s^{-1} accretion rate trajectory.

during the 32×10^{-5} $M_\odot$ s^{-1} accretion rate was analysed. Fig. 13 shows the evolution of several alpha capture products, as well as ^{13,14}N. At the start of the trajectory, during the plateau phase when the temperature is 0.25 GK, the CNO cycle is the main source of nucleosynthesis. This is shown in Fig. 13 by the rapid increase of ^{13}N early in the time evolution. As the temperature climbs, from 0.25 GK to 4.3 GK at the peak, the fraction of ^{13}N drops by several orders of magnitude as the CNO cycle is no longer the preferred reaction pathway. As ^{12}C drops the mass fraction of ^{24}Mg begins to increase, indicating that alpha capture reactions are bypassing the CNO cycle. This is supported by the rise in the ^{44}Ti mass fraction as the temperature rises, indicating the alpha capture process is moving material up towards the iron group. Following the peak temperature, ^{4}He has been completed depleted and ^{56}Ni has the highest mass fraction of all isotopes. As we move down the alpha capture products, there is less mass in each isotope.

Table 2 shows that there is a strong inverse relationship between the production of ^{44}Ti and ^{56}Ni when the neutron star accretes material at this accretion rate. For material with a large disc ejection radius, where the peak temperature reached is lower, alpha capture chains produce high fractions of ^{44}Ti but cannot produce significant amounts of ^{56}Ni. Comparatively, material which has a small disc ejection radius, where higher peak temperatures occur, undergoes alpha captures up to ^{56}Ni, burning ^{44}Ti to do so. Of the total amount of ^{44}Ti ejected from the accretion disc at this accretion rate, 99.9 per cent is ejected at in the three outermost ejection radii while less than 1 per cent of the total ^{56}Ni is ejected at these radii. The inner five ejection radii containing 99.5 per cent of the total ^{56}Ni mass fraction, but less than 1 per cent of the ^{44}Ti mass fraction.There is no disc ejection radius which ejects significant amounts of both ^{44}Ti and ^{56}Ni. ^{44}Ti and ^{56}Ni are both known gamma-ray observable isotopes (S. Andrews et al. 2020).

This has implications for potential observations of accreting neutron star CE remnants. The mechanism by which the stellar envelope is ejected at the end of the CE phase remains an active area of investigation. However, outflows driven by the neutron star accretion disc may contribute to the ejection of the shared envelope. Table 2 shows the ejection velocity of material leaving the disc. This, in context of the inverse relationship between ^{44}Ti and ^{56}Ni, indicates that the ^{56}Ni will be ejected faster than the ^{44}Ti. This may lead to a CE remnant with a high concentration of ^{44}Ti near the centre, and a high concentration of ^{56}Ni further out. If these outflows power supernova-like outbursts, one way to distinguish them would to compare the ^{56}Ni and ^{44}Ti line profiles (a.k.a. the velocity distribution of the lines).

6.3 Helium core region

As the neutron star inspirals further into the core of the companion star, it begins accreting helium-rich material. The initial composition of this environment consists of 93.4 per cent ^{4}He and only 0.45 per cent ^{2}H. For all three companion stars explored in this work, the neutron star accretes material from the helium core at an accretion rate between 4×10^{-5} and 512×10^{-5} $M_\odot$ s^{-1} (see Figs 3, A1, and A2). The composition of the material accreted varies between the three companion stars: The 20.3$R_\odot$ companion has mass fractions of ^{12}C of the order of 10^{-4}, as the star continues to evolve to reach stellar radii of 52.4 $R_\odot$ and then 275.6 $R_\odot$, the mass fraction of ^{12}C increases from 10^{-4} to 10^{-3}. The larger fraction of ^{12}C provides a higher fraction of seed nuclei for alpha capture reactions, resulting in higher fractions of alpha capture products. When the neutron star accretes material at 16×10^{-5} $M_\odot$ s^{-1}, there is evidence of neutron capture reactions. Fig. 14 shows the final isotopic mass fraction distribution averaged over all ejection points across the accretion disc for the 16×10^{-5} $M_\odot$ s^{-1} accretion rate inside the 52.4 $R_\odot$ companion (Fig. A1). The high fraction of helium results in alpha capture reactions dominating nucleosynthesis, similar in Fig. 12. However, there is also a high enough flux of neutrons produced that neutron capture reactions occur and produce trace mass fractions of isotopes on the neutron-rich side of the valley of stability. This high neutron flux originates in a combination of (α, n) reactions, which compete with (α, p) and (α, γ) reactions in the low-mass region, and neutron emissions from heavy isotopes due to photodisintegration reactions at high temperatures.

The highest accretion rate the neutron star accretes material at is 512×10^{-5} $M_\odot$ s^{-1} when the companion has expanded to 52.4 $R_\odot$ (see Fig. A1). Trajectories at this accretion rate reach temperatures and densities well into the expected range for nuclear statis-

Downloaded from academic.oup.com/mnras/article/552/4/stag1751/8869235 by guest on 16 October 2026

Table 2. Mass fraction of ^{44}Ti and ^{56}Ni ejected at each point throughout the accretion disc at the end of the 32×10^{-5} $M_\odot$ s^{-1} accretion rate trajectory.

Disc ejection radius ($\times 10^6$ cm)	Mass fraction of ^{44}Ti	Mass fraction of ^{56}Ni	Peak temperature (GK)	Ejection velocity (m s^{-1})
1.04	2.09×10^{-7}	9.02×10^{-1}	6.21	1.96×10^{8}
1.30	3.33×10^{-7}	9.15×10^{-1}	5.97	1.75×10^{8}
1.63	5.32×10^{-7}	9.32×10^{-1}	5.47	1.56×10^{8}
2.04	2.16×10^{-5}	7.48×10^{-1}	4.36	1.40×10^{8}
2.54	2.37×10^{-4}	2.56×10^{-2}	3.15	1.25×10^{8}
3.11	1.13×10^{-2}	1.05×10^{-2}	2.58	1.13×10^{8}
3.98	2.26×10^{-2}	6.08×10^{-3}	2.27	1.00×10^{8}
4.97	1.55×10^{-1}	2.30×10^{-4}	2.04	8.95×10^{7}

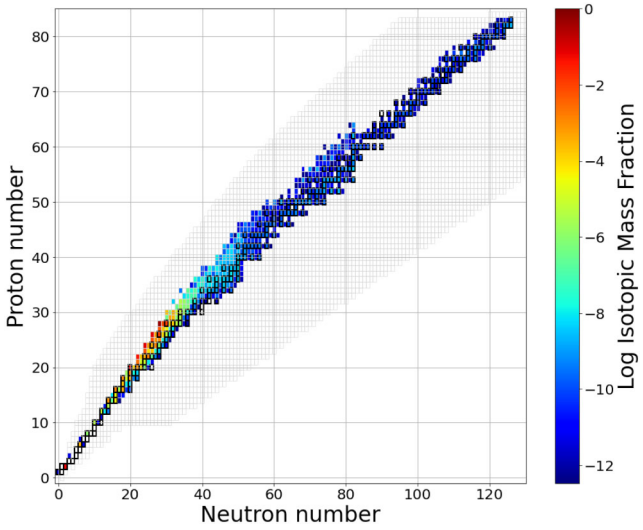


Figure 14. Final isotopic mass fractions averaged over all points of ejection for the 16×10^{-5} $M_\odot$ s^{-1} accretion rate inside the 52.4 $R_\odot$ companion.

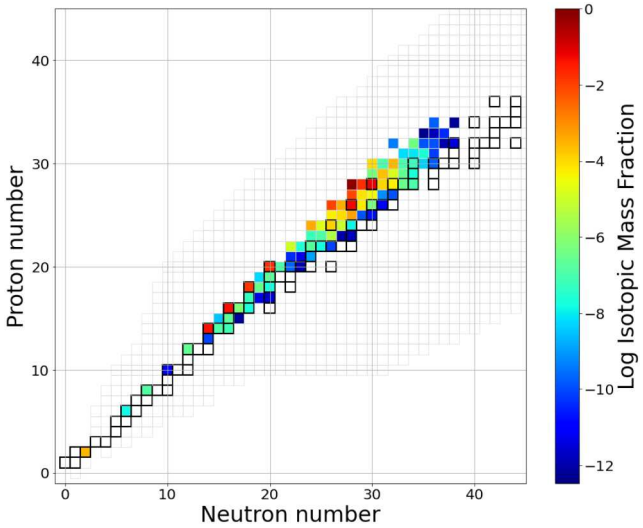


Figure 15. Average undecayed final isotopic distribution for the 512×10^{-5} $M_\odot$ s^{-1} accretion rate trajectory. Peak temperatures reached in this trajectory range between 4.07 and 8.72 GK.

tical equilibrium. The resulting isotopic distribution for material accreted into the neutron star accretion disc at 512×10^{-5} $M_\odot$ s^{-1} is shown in Fig. 15. Nucleosynthesis does not reach significantly beyond the iron group elements, and ^{56}Ni has the highest mass fraction. At these extreme temperatures, the reaction pathways that produce the most stably bound nuclei are favoured. This results in high mass fractions of iron group elements. All accretion rates that exceed 100×10^{-5} $M_\odot$ s^{-1} produce iron group elements. This is due to the composition of the accreted material and the extreme temperatures inside the neutron star accretion disc reached as the neutron star inspirals into the helium core. Alpha capture chains produce material up to ^{56}Ni but cannot continue further. When the neutron star accretes material at 512×10^{-5} $M_\odot$ s^{-1}, the conditions inside the disc for many of the ejection radii are within the expected NSE temperature range, regardless of the companion star's age.

7 CONCLUSIONS

From the results shown in section 5, we can see that the full initial composition is essential to modelling nucleosynthesis in the neutron star accretion disc during CE. If the full range of seed nuclei are not included, then the nucleosynthesis observed is limited, as seen in Fig. 4, and does not accurately represent the nucleosynthetic processes that occur as material moves through the neutron star accretion disc.

The results of this investigation show that the neutron star accretion disc within a CE can produce a variety of types of nucleosynthesis. If material is accreted from the hydrogen-rich outer shells, then material in the neutron star accretion disc will undergo rapid proton captures due to the high availability of free protons and the gigakelvin temperatures reached during accretion (see Figs 5–8).

If the orbital separation between the neutron star and companion is sufficiently small to form a CE where the neutron star accretion disc forms within the mixed hydrogen and helium shell, alpha capture reactions dominate the low-mass region up to the iron group. The iron group products then capture protons to produce neutron deficient intermediate mass elements (see Figs 11 and 12). Nucleosynthesis does not reach the end point of the rp-process.

If the neutron star accretes helium-rich material from the centre of the companion star, it can do so at a range of accretion rates. If the neutron star is towards the outer edge of the helium core, then nucleosynthesis can produce trace amounts of neutron-rich isotopes close to stability. If the neutron star reaches the centre of the helium core, then the material in the accretion disc experiences extreme temperatures (greater than 5 GK) for enough time to undergo nuclear statistical equilibrium. At these temperatures, the material form iron group elements as these have the lowest nuclear binding energy (see Fig. 15).

Overall, a variety of nucleosynthetic processes can occur within a neutron star accretion disc within a CE, with their

Downloaded from academic.oup.com/mnras/article/552/4/stag1751/8869235 by guest on 16 October 2026

products subsequently mixed back into the companion star via wind-driven ejection. At the end of CE evolution, this material may be ejected into the interstellar medium and contribute to galactic chemical evolution.

The inclusion of angular momentum is essential in accurately modelling the neutron star accretion disc within the CE. When the angular momentum of the accreting material is not included, such as the work conducted by J. Keegans et al. (2019), the timescale for accretion and ejection is much shorter and so the time in which the material can undergo nucleosynthesis is extremely short. When the angular momentum is included, the material must shed this before it can move further through the accretion disc. This results in the long disc evolution stage and the temperature plateau seen in Fig. 1. The disc evolution stage provides a site for CNO and CNO breakout reactions to occur, producing higher fractions of isotopes below the iron peak and providing a larger fraction of seed nuclei to undergo nucleosynthesis at the peak temperature of the trajectory. In particular, the long disc evolution stage allows for seed nuclei in the accreted material to undergo the rp-process. This leads to the ejection of neutron deficient isotopes from the neutron star accretion disc, with potential for them to be ejected into the interstellar medium and contribute to galactic chemical evolution. We found decreasing the angular momentum of the material accreted increases the time spent in the outer region of the accretion disc, and so varies the time spent at the plateau temperature. As the isotopic yields are most sensitive to the peak temperature, this results in variation in the CNO and CNO break out isotopes produced during the plateau temperature, but the final mass fraction variations follow the same trends seen in the high angular momentum case.

We find that ^{44}Ti is produced in the outer regions of the accretion disc while ^{56}Ni is produced in the inner regions of the disc, and that the ejection velocity of these isotopes varies (see Table 2). If CE events produce supernova-like outbursts, the differences in the abundances may be the primary way to distinguish these events from other supernova engines. For example, since ^{56}Ni is primarily produced in the inner disc where ejection velocities are higher whereas ^{44}Ti is produced further out, we would expect the iron (which is the decay product of ^{56}Ni) in this type of transient remnant to be further out than the ^{44}Ti. This is currently seen in the Cassiopeia A remnant, but note that there are other aspects of Cassiopeia A that suggest a convective engine (B. W. Grefenstette et al. 2014). Measuring the velocity distribution in the ^{44}Ti lines in Supernova 1987A and comparing it to the ^{56}Ni lines will also allow scientists to determine whether this supernova was CE driven. Abundances can be a powerful engine diagnostic.

ACKNOWLEDGEMENTS

ADH-S, SEDA, AML, and CAD acknowledge support from the Science and Technology Funding Council through grants ST/V001035/1 and ST/Y000285/1. The work by CLF and SWJ was supported by the U.S. Department of Energy through the Los Alamos National Laboratory. Los Alamos National Laboratory is operated by Triad National Security, LLC, for the National Nuclear Security Administration of U.S. Department of Energy (Contract No. 89233218CNA000001). The authors thank the NuGrid team for useful discussions and code support (LA-UR-26-21365).

DATA AVAILABILITY

The data used in this project and all associated data are available upon reasonable request to the corresponding author.

REFERENCES

Abrahams S. E. D., Fryer C., Hall-Smith A., Laird A., Diget C., 2023, in Freeman S., Lederer-Woods C., Manna A., Mengoni A., eds, EPJ Web Conf. Vol. 2789, Nuclear Physics in Astrophysics - X (NPA-X 2022). EPJ, Geneva, Switzerland, p. 10002
Andrews S., Fryer C., Even W., Jones S., Pignatari M., 2020, ApJ, 890, 35
Anninos P., Portman M. E., Carmichael S. R., Hoffman R. D., Sieverding A., 2026, ApJ, 997, 88
Bondi H., 1952, MNRAS, 112, 195
Chevalier R. A., 1989, ApJ, 346, 847
Chevalier R. A., 1993, ApJ, 411, L33
Cyburt R. H. et al., 2010, ApJS, 189, 240
Dillmann I., Heil M., Käppeler F., Plag R., Rauscher T., Thielemann F.-K., 2008, preprint (arXiv:0805.4749)
Everson R. W., MacLeod M., De S., Macias P., Ramirez-Ruiz E., 2020, ApJ, 899, 77
Fröhlich C. et al., 2005, Nucl. Phys. A, 758, 27
Fryer C. L., Woosley S. E., 1998, ApJ, 502, L9
Fryer C. L., Woosley S. E., Hartmann D. H., 1999, ApJ, 526, 152
Fryer C. L., Herwig F., Hungerford A., Timmes F. X., 2006, ApJ, 646, L131
Fryer C. L., Belczynski K., Berger E., Thöne C., Ellinger C., Bulik T., 2013, ApJ, 764, 181
Grefenstette B. W. et al., 2014, Nature, 506, 339
Hillel S., Schreier R., Soker N., 2022, MNRAS, 514, 3212
Iliadis C., 2007, Nuclear Physics of Stars. Wiley-VCH Verlag, Wenheim, Germany
Ivanova N., Heinke C. O., Rasio F. A., Belczynski K., Fregeau J. M., 2008, MNRAS, 386, 553
Ivanova N. et al., 2013, A&AR, 21, 59
Ivanova N., Justham S., Ricker P., 2020, Common Envelope Evolution. IOP Publishing, Bristol, UK
Juarez-Garcia A. L., De Marco O., De Colle F., López-Cámara D., Moreno Méndez E., Carrillo-Santamaría J., Wardle M., 2025, PASA, 42, e076
Kaltenborn M. A. R., Fryer C. L., Wollaeger R. T., Belczynski K., Even W., Kouveliotou C., 2023, ApJ, 956, 71
Keegans J. et al., 2019, MNRAS, 485, 620
Klencki J., Metzger B. D., 2026, ApJ, 1005, 2
Langanke K., Martínez-Pinedo G., 2000, Nucl. Phys. A, 673, 481
MacLeod M., Ramirez-Ruiz E., 2015, ApJ, 798, L19
Meng X., Podsiadlowski P., 2017, MNRAS, 469, 4763
Neights E. et al., 2026, MNRAS, 545, staf2019
Oda T., Hino M., Muto K., Takahara M., Sato K., 1994, At. Data Nucl. Data Tables, 56, 231
Parikh A., José J., Moreno F., Iliadis C., 2008, ApJS, 178, 110
Passy J.-C. et al., 2012, ApJ, 744, 52
Pignatari M. et al., 2016, ApJS, 225, 24
Popham R., Woosley S. E., Fryer C., 1999, ApJ, 518, 356
Ragoler N., Bear E., Schreier R., Hillel S., Soker N., 2022, MNRAS, 515, 5473
Ritter C., Herwig F., Jones S., Pignatari M., Fryer C., Hirschi R., 2018, MNRAS, 480, 538
Ruffert M., Anzer U., 1995, A&A, 295, 108
Schreier R., Hillel S., Soker N., 2025, Open J. Astrophys., 8, 60
Shakura N. I., Sunyaev R. A., 1973, A&A, 24, 337
Sieverding A., Kresse D., Janka H.-T., 2023, ApJ, 957, L25
Surman R., McLaughlin G. C., Hix W. R., 2006, ApJ, 643, 1057
Thöne C. C. et al., 2011, Nature, 480, 72
Vetter M., Röpke F. K., Schneider F. R. N., Pakmor R., Ohlmann S. T., Lau M. Y. M., Andrassy R., 2024, A&A, 691, A244
Zhang W., Fryer C. L., 2001, ApJ, 550, 357

Downloaded from academic.oup.com/mnras/article/552/4/stag1751/8869235 by guest on 16 October 2026

APPENDIX A: ADDITIONAL FIGURES

Fig. A1 shows the mass fraction of ^{2}H, ^{4}He, ^{12}C, ^{14}N, and ^{16}O as a function of the 15 $M_{\odot}$ companion radius when the star has expanded to 52.5 $R_{\odot}$. The accretion rate as a function of companion radius is also shown. From this, the initial composition for each accretion rate in each environment can be accurately calculated.

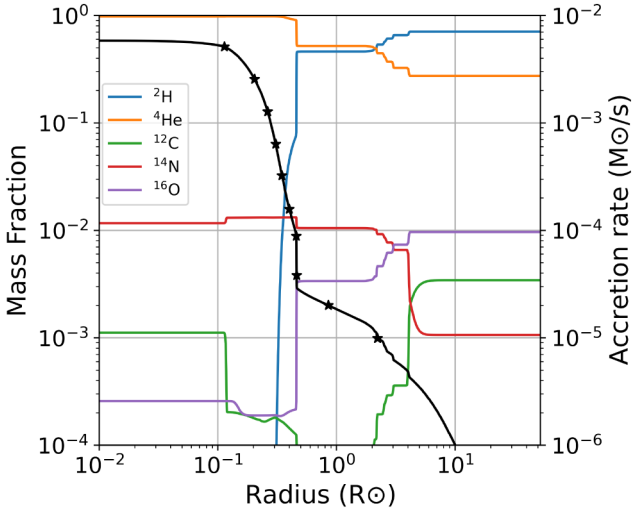


Figure A1. Composition of a 15 $M_{\odot}$ ZAMS star, when it has expanded to 52.4 $R_{\odot}$. The mass fraction (left axis) for ^{2}H, ^{4}He, ^{12}C, ^{14}N, and ^{16}O shown as a function of radial distance from the companion core. Also shown is the accretion rate (right axis) in solar masses per second versus radial distance. Black asterisks indicate accretion rates used in current study.

Fig. A2 shows the mass fraction of ^{2}H, ^{4}He, ^{12}C, ^{14}N, and ^{16}O as a function of the 15 $M_{\odot}$ companion radius when the star has expanded to 275.6 $R_{\odot}$. The accretion rate as a function of companion radius is also shown.

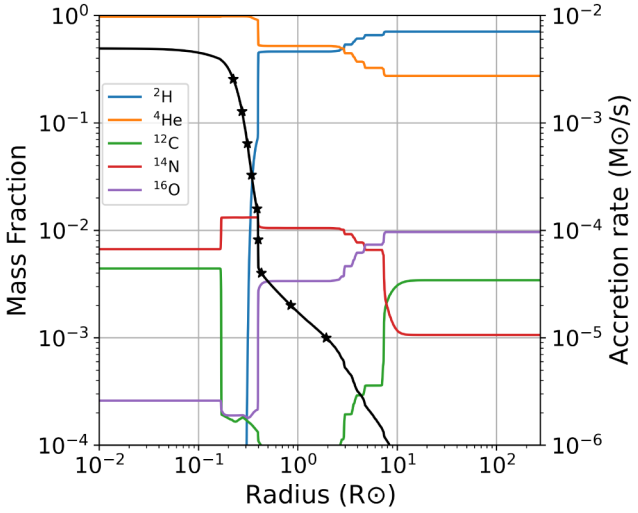


Figure A2. Composition of a 15 $M_{\odot}$ ZAMS star, when it has expanded to 275.6 $R_{\odot}$. The mass fraction (left axis) for ^{2}H, ^{4}He, ^{12}C, ^{14}N, and ^{16}O shown as a function of radial distance from the companion core. Also shown is the accretion rate (right axis) in solar masses per second versus radial distance. Black asterisks indicate accretion rates used in current study.

This paper has been typeset from a TEX/LATEX file prepared by the author.

Downloaded from academic.oup.com/mnras/article/552/4/stag1751/8869235 by guest on 16 October 2026

© The Author(s) 2026.
Published by Oxford University Press on behalf of Royal Astronomical Society. This is an Open Access article distributed under the terms of the Creative Commons Attribution License (https://creativecommons.org/licenses/by/4.0/), which permits unrestricted reuse, distribution, and reproduction in any medium, provided the original work is properly cited.